

1  
2  
3  
4  
5  
6  
7  
8  
9 **Diapycnal mixing across the photic zone of the**  
10 **NE-Atlantic**

11  
12  
13  
14  
15  
16 by **Hans van Haren<sup>\*</sup>, Corina P.D. Brussaard, Loes J. A.**  
17 **Gerringa, Mathijs H. van Manen, Rob Middag,**  
18 **Ruud Groenewegen**

19  
20  
21  
22  
23  
24  
25  
26  
27  
28  
29  
30  
31  
32  
33  
34  
35  
36  
37  
38  
39 Royal Netherlands Institute for Sea Research (NIOZ), P.O. Box 59, 1790 AB Den Burg,  
40 the Netherlands.

41 \*e-mail: [hans.van.haren@nioz.nl](mailto:hans.van.haren@nioz.nl)

44 **Abstract.** Variable physical conditions such as vertical turbulent exchange, internal wave and  
45 mesoscale eddy action, affect the availability of light and nutrients for phytoplankton  
46 (unicellular algae) growth. It is hypothesized that changes in ocean temperature may affect  
47 ocean vertical density stratification, which may hamper vertical exchange. In order to quantify  
48 variations in physical conditions in the Northeast Atlantic Ocean, we sampled a latitudinal  
49 transect along  $17\pm 5^{\circ}\text{W}$  between  $30^{\circ}$  and  $63^{\circ}\text{N}$  in summer. A shipborne Conductivity-  
50 Temperature-Depth CTD-instrumented package was used with a custom-made modification of  
51 the pump-inlet to minimize detrimental effects of ship motions on its data. Thorpe-scale  
52 analysis was used to establish turbulence values for the upper 500 m ~~near the surface~~ from 3 to  
53 6 profiles obtained in a short CTD-yoyo, 3 to 5 h after local sunrise. From south to north,  
54 average temperature decreased together with stratification while turbulence values weakly  
55 increased or remained constant. Vertical turbulent nutrient fluxes did not vary significantly with  
56 stratification and latitude. This apparent lack of correspondence between turbulent mixing and  
57 temperature is likely due to internal waves breaking (increased stratification can support more  
58 internal waves), acting as a potential feed-back mechanism. As this feed-back mechanism  
59 mediates potential physical environment changes in temperature, global surface ocean warming  
60 may not affect the vertical nutrient fluxes to a large degree. We urge modelers to test this  
61 deduction as it could imply that the future summer phytoplankton productivity in stratified  
62 oligotrophic waters would experience little alterations in nutrient input from deeper waters.  
63  
64

65 **1 Introduction**

66 The physical environment is important for ocean life, including variations therein. For  
67 example, the sun stores heat in the ocean with a stable vertical density stratification as result.  
68 Generally, stratification hampers vertical turbulent exchange because of the required work  
69 against (reduced) gravity before turbulence can take effect. It thus hampers a supply of nutrients  
70 via a turbulent flux from deeper waters to the photic zone. However, stratification supports  
71 internal waves, which (i) may move near-floating particles like phytoplankton (unicellular  
72 algae) up- and down towards and away from the surface, and (ii) may induce enhanced  
73 turbulence via vertical current differences (shear) resulting in internal waves breaking (Denman  
74 and Gargett, 1983). Such changes in the physical environment are expected to affect the  
75 availability of phytoplankton growth factors such as light and nutrients.

76 Climate models predict that global warming will reduce vertical mixing in the oceans (e.g.,  
77 Sarmiento et al., 2004). Mathematical models on system stability suggest that reduced mixing  
78 may generate chaotic behaviour in phytoplankton production, thereby enhancing variability in  
79 carbon export into the ocean interior (Huisman et al., 2006). However, none of these models  
80 include potential feed-back systems like internal wave action or mesoscale eddy activity. From  
81 observations in the relatively shallow North Sea it is known that the strong seasonal temperature  
82 stratification is marginally stable, as it supports internal waves and shear to such extent that  
83 sufficient nutrients are replenished from below to sustain the late-summer phytoplankton bloom  
84 in the euphotic zone that became depleted of nutrients after the spring bloom (van Haren et al.,  
85 1999). This challenges the current paradigm in climate models.

86 In this paper, the objective is to resolve the effect of vertical stratification and turbulent  
87 mixing on nutrient supply to the euphotic zone of the open ocean. For this purpose, upper-500-  
88 m-ocean shipborne Conductivity-Temperature-Depth CTD-observations were made in  
89 association with those on dissolved inorganic nutrients during a survey along a transect in the  
90 NE-Atlantic Ocean from mid-(30°) to high-(63°) latitudes in summer. Throughout the survey,  
91 meteorological and sea-state conditions were favourable for adequate sampling and wind

92 speeds varied little between 5 and 10 m s<sup>-1</sup>, independent of locations. All CTD-observations  
93 were made far from lateral, continental boundaries and at least 1000 m vertically away from  
94 bottom topography (i.e. far from internal-tide sources). The NE-Atlantic is characterized by  
95 abundant (sub-)mesoscale eddies especially in the upper ocean (Charria et al., 2017) that  
96 influence local plankton communities (Hernández- Hernández et al., 2020). The area also  
97 shows continuous abundant internal wave activity away from topographic sources and sinks,  
98 with the semidiurnal tide as a main source from below and atmospherically induced inertial  
99 motions from above (e.g., van Haren, 2005; 2007). However, the sampled upper 500-m zone  
100 transect is not known to demonstrate outstanding internal wave source variations. Previous  
101 observations (van Haren, 2005) and Hibiya et al. (2007) have shown that a diurnal critical  
102 latitude enhancement of near-inertial internal waves due to subharmonic instability only occurs  
103 sharply between 25 and 30°N. The present observations are all made poleward of this range.  
104 Likewise, the Henyey et al. (1986) model on latitudinal variation of internal wave energy and  
105 turbulent mixing (Gregg et al., 2003) predicts changes by a factor of maximum 1.8 between  
106 30° and 63°, but this value is relatively small compared with errors, typically a factor of 2 to 3,  
107 in turbulence dissipation rate observations. Likewise, from the equal summertime  
108 meteorological conditions little variation is expected in the generation of upper ocean near-  
109 inertial internal waves. Naturally, other processes like interaction between internal waves and  
110 mesoscale phenomena may be important locally, but these are expected to occur in a similar  
111 fashion across the sampled ocean far away from boundaries. Thus, the sampled dataset is  
112 considered adequate for a discussion on the variability of turbulence, stratification and vertical  
113 turbulent nutrient fluxes with latitude.

114 The present research complements research based on photic zone (upper 100 m)  
115 observations obtained along the same transect using a slowly descending turbulence  
116 microstructure profiler next to CTD-sampling eight years earlier (Jurado et al., 2012). Their  
117 data demonstrated a negligibly weak increase in turbulence values with significant decreases in  
118 stratification going north. However, no nutrient data were presented and no turbulent nutrient

119 fluxes could be computed. In another summertime study (Mojica et al., 2016), macro-nutrient  
120 concentrations indicated oligotrophic conditions along the same latitudinal transect but the  
121 vertical gradients for the upper 200 m showed an increase from south to north. The present  
122 observations go deeper to 500 m, also across the non-seasonal more permanent stratification.  
123 Moreover, coinciding measurements were made of the distributions of macro-nutrients and  
124 dissolved iron. This allows vertical turbulent nutrient fluxes to be computed. It leads to a  
125 hypothesis concerning a physical feed-back mechanism that may control changes in  
126 stratification.

127

## 128 **2 Materials and Methods**

129 Between 22 July and 16 August 2017, observations were made from the R/V Pelagia in the  
130 Northeast Atlantic Ocean at stations along a transect from Iceland, starting around 60°N, to the  
131 Canary Islands, ending at 30°N, (Fig. 1). The transect was roughly-more or less in meridional  
132 direction, with stations along 17±5°W, all in the same time zone (UTC-1 h = local time LT).  
133 Full water-depth Rosette bottle water sampling was performed at most stations.

134 Samples for dissolved inorganic macro-nutrients were filtered through 0.2 µm Acrodisc  
135 filter and stored frozen in a high-density polyethylene**HDPE** pony-vial (nitrate, nitrite and  
136 phosphate) or at 4°C (silicate) until analysis. Nutrients were analysed under temperature  
137 controlled conditions using a QuAAstro Gas Segmented Continuous Flow Analyser. All  
138 measurements were calibrated with standards diluted in low nutrient seawater in the salinity  
139 range of the stations to ensure that analysis remained within the same ionic strength. Phosphate  
140 ( $\text{PO}_4$ ), nitrate plus nitrite ( $\text{NO}_x$ ), were measured according to Murphy and Riley (1962) and  
141 Grasshoff et al. (1983), respectively. Silicate was analysed using the procedure of Strickland  
142 and Parsons (1968).

143 Absolute and relative precision were regularly determined for reasonably high  
144 concentrations in an in-house standard. For phosphate, the standard deviation was 0.028 µM  
145 ( $N = 30$ ) for a concentration of 0.9 µM; Hence the relative precision was 3.1%. For nitrate, the

146 values were 0.14  $\mu\text{M}$  ( $N = 30$ ) for a concentration of 14.0  $\mu\text{M}$ , so that the relative precision was  
147 1.0%. For silicate, the values were 0.09  $\mu\text{M}$  ( $N = 15$ ) for a concentration of 21.0  $\mu\text{M}$ , so that  
148 the relative precision was 0.4%. The detection limits were 0.007, 0.012 and 0.008  $\mu\text{M}$ , for  
149 phosphate, nitrate and silicate, respectively.

150 For dissolved iron samples, the ultraclean “Pristine” sampling system for trace metals was  
151 used (Rijkenberg et al., 2015). All bottles used for storage of reagents and samples were cleaned  
152 according to an intensive three step cleaning protocol described by Middag et al. (2009).  
153 Dissolved iron concentrations were measured shipboard using a Flow Injection—  
154 Chemiluminescence method with preconcentration on iminodiaceticacid-~~IDA~~ resin as  
155 described by De Baar et al. (2008) and modified by Klunder et al. (2011). In order to validate  
156 the accuracy of the system, standard reference seawater (SAFe) was measured regularly in  
157 triplicate (Johnson et al. 1997).

158 At 19 out of 32 stations a yoyo consisting of 3 to 6 casts, totaling 72 casts, of electronic  
159 CTD profiles was done to monitor the temperature-salinity variability and to establish turbulent  
160 mixing values from 5 to 500 m below the ocean surface. The yoyo casts were made  
161 consecutively and took between 1 and 2 hours per station. They were mostly obtained in the  
162 morning: at ten stations between 6 and 8 LT, at eight stations between 8 and 10 LT, and at one  
163 station in the afternoon, around noon. As the observations were made in summer, the latitudinal  
164 difference in sunrise was 1.5 h between the northernmost (earlier sunrise) and southernmost  
165 stations. This difference is taken into account and sampling times are referenced to time after  
166 local sunrise. It is assumed that the stations sampled just after sunrise ~~more or less~~ reflect the  
167 upper ocean conditions of (late-) nighttime cooling convection so that vertical near-  
168 homogeneity was at a maximum, and near-surface stratification at a minimum, while the late  
169 morning and afternoon stations reflected daytime stratifying near-surface conditions due to the  
170 stabilizing solar insolation.

171

172 **2.1 Instrumentation and modification**

173 A calibrated SeaBird 911plus CTD was used. The CTD data were sampled at a rate of 24  
174 Hz, whilst lowering the instrumental package at a speed of  $1 \text{ m s}^{-1}$ . The data were processed  
175 using the standard procedures incorporated in the SBE-software, including corrections for cell  
176 thermal mass (Lueck, 1990) using the parameter setting of Mensah et al. (2009) and sensor  
177 time-alignment. All other analyses were performed using Conservative Temperature ( $\Theta$ ),  
178 ~~Absolute Salinity  $S_A$  and potential density anomalies  $\sigma_0$ , with  $1000 \text{ kg m}^{-3}$  subtracted from~~  
179 ~~total density and -referenced to the surface for pressure corrections as vertical profiles were~~  
180 ~~only analyzed shallower than 600 m~~, using the Gibbs SeaWater-software (IOC, SCOR, IAPSO,  
181 2010).

182 Observations were made with the CTD upright rather than horizontal in a lead-weighted  
183 frame without water samplers to minimize artificial turbulent overturning. Variable speeds of  
184 the flow passing the temperature and conductivity sensors will cause artificial temperature and  
185 thus apparent turbulent overturning, noticeable in near-homogeneous waters such as found near  
186 the surface during nighttime convection. To eliminate variable flow speeds, a custom-made  
187 assembly with pump in- and outlet tubes and tube-ends of exactly the same diameter was  
188 mounted to the CTD as described in van Haren and Laan (2016). This reduces frictional  
189 temperature effects of typically  $\pm 0.5 \text{ mK}$  due to fluctuations in pump speed of  $\pm 0.5 \text{ m s}^{-1}$  when  
190 standard SBE-tubing is used (Appendix A1). The effective removal of the artificial temperature  
191 effects using the custom-made assembly is demonstrated in Fig. 2, in which surface wave action  
192 via ship motion is visible in the CTD-pressure record, but not in its temperature variations  
193 record. For example, at station 32 the CTD was lowered in moderate sea state conditions with  
194 surface waves of maximum 2 m crest-trough. The surface waves are recorded by pressure  
195 variations as a result of ship motions (Fig. 2a). In the upper ~~3540~~ m near the surface, the waters  
196 were partially unstable and partially near-homogeneous, with temperature variations well  
197 within  $\pm 0.5 \text{ mK}$  and high-frequency variations O(0.1) mK (Fig. 2b). The  $\Delta T$ -variations did not  
198 vary with the surface wave periodicity of about 10 s. No correlation was found between data  
199 in Fig. 2b and Fig. 2a. This effective removal of ship motion in CTD-temperature data is

Formatted: Subscript

Formatted: Superscript

200 confirmed for the entire 500 m depth-range in average spectral information (Fig. 2c-e). In the  
201 power spectra, the pressure gradient  $dp/dt \sim$  CTD-velocity shows a clear peak around 0.1 cps,  
202 short for cycles per s, which correspond to a period of 10 s. Such a peak is absent in both spectra  
203 of temperature T and density anomaly referenced to the surface  $\sigma_0$ . The correlation between  
204  $dp/dt$  and T is not significantly different from zero (Fig. 2d,e). With conventional tubing and  
205 tube-ends, the surface wave variations would show in such  $\Delta T$ -graph (van Haren and Laan,  
206 2016). Without the effects of ship motions, considerably less corrections need to be applied for  
207 turbulence calculations (see below).

208

## 209 **2.2 Ocean turbulence calculation**

210 Turbulence is quantified using the analysis method by Thorpe (1977) on potential density  
211 ( ~~$\sigma_0$~~ ) inversions of less dense water below a layer of denser water in a vertical (z) profile. Such  
212 inversions are interpreted as turbulent overturns of mechanical energy mixing. Vertical  
213 turbulent kinetic energy dissipation rate ( $\varepsilon$ ) is a measure of the amount of kinetic energy put in  
214 a system for turbulent mixing. It is proportional to the magnitude of turbulent diapycnal flux  
215 (of potential density)  $|K_z d\sigma_0/dz|$ . In practice it is determined by calculating overturning scales  
216 with magnitude  $|d|$ , just like turbulent eddy diffusivity ( $K_z$ ). The vertical potential density  
217 stratification is indicated by  $d\sigma_0/dz$ . The turbulent overturning scales are obtained after  
218 reordering the measured potential density profile  $\sigma_0(z)$ , which may contain inversions, into a  
219 stable monotonic profile  $\sigma_0(z_s)$  without inversions (Thorpe, 1977). After comparing raw and  
220 reordered profiles, displacements  $d = \min(|z-z_s|) \cdot \text{sgn}(z-z_s)$  are calculated that generate the stable  
221 profile. Then, using root-mean-square displacement value  $L_T = \text{rms}(d)$  computed over certain - - - - - Formatted: Subscript  
222 vertical scales (see below). - - - - - Formatted: Subscript

223 
$$\varepsilon = 0.64 \frac{L_T^2}{4} N^3 \quad [\text{m}^2 \text{s}^{-3}], \quad (1)$$
 - - - - - Formatted: Subscript

224 where  $N = \{ -g/\rho(d\sigma_0(z_s)/dz) \}^{1/2} = \{ g/\rho(d\rho/dz + g\rho/\varepsilon_s^2) \}^{1/2}$  (e.g., Gill, 1982). - - - - - Formatted: Subscript  
225 denotes the buoyancy frequency (~ square-root of stratification as is clear from the equation) computed from the  
226 reordered profile. Here, g is the acceleration of gravity and  $\rho = 1027 \text{ kg m}^{-3}$  denotes the - - - - - Formatted: Superscript

227 reference density. We like to note, following previous warnings by, e.g., Gill (1982) and King  
228 et al. (2012), that our definition of  $N$  is a practical one, which should not be used for data from  
229 deeper waters. For deeper waters, density should be referenced to a local pressure reference  
230 level, which effectively implies the use of the exact definition for buoyancy frequency as  
231 formulated, e.g., by Gill (1982):  $\{-g/\rho(d\rho/dz + gp/c_s^2)\}^{1/2}$ , where ~~Here,  $g$  is the acceleration of~~  
232 ~~gravity and  $c_s$  is~~ the speed of sound reflecting pressure-compressibility effects. ~~Our ‘surface~~  
233 ~~waters’  $N$  computed over reordered profiles only negligibly deviates from above exact  $N$  and~~  
234 ~~corresponds with  $N$  computed from raw profiles~~ over a typical vertical length-scale of  $\Delta z =$   
235 100 m, ~~which more or less~~ This  $\Delta z$  represents the scales of large internal waves that are  
236 supported by the density stratification ~~and of the largest turbulent overturns.~~

237 The numerical constant of 0.64 in (1) follows from empirically relating the overturning scale ~~to~~ Formatted: Indent: First line: 0.2"  
238 magnitude with the Ozmidov scale  $L_O$  of largest possible turbulent overturn in a stratified flow:

239  $(L_O/L_{\text{Ozmidov}})^{0.8}$  (Dillon, 1982), a mean coefficient value from many realizations. Using  $K_z =$  Formatted: Subscript  
240  $\Gamma \varepsilon N^2$  and a mean mixing efficiency coefficient of  $\Gamma = 0.2$  for the conversion of kinetic into  
241 potential energy for ocean observations that are suitably averaged over all relevant turbulent  
242 overturning scales of the mix of shear-, current differences, and convective, buoyancy driven,  
243 turbulent overturning in large Reynolds number flow conditions (e.g., Osborn, 1980; Oakey,  
244 1982; Ferron et al., 1998; Gregg et al., 2018), we find,

245 
$$K_z = 0.128 L_{\text{Ozmidov}}^2 N \quad [\text{m}^2 \text{s}^{-1}] \quad (2)$$
 Formatted: Subscript

246 This parametrization is also valid for the upper ocean, as has been shown extensively by Oakey  
247 (1982) and recently confirmed by Gregg et al. (2018). The inference is that the upper ocean  
248 may be weakly stratified at times, but stratification and turbulence vary considerably with time  
249 and space. Sufficient averaging collapses coefficients to the mean values given above. This is  
250 confirmed in recent numerical modeling by Portwood et al. (2019).

251 As  $K_z$  is a mechanical turbulence coefficient it is not property-dependent like a molecular  
252 diffusion coefficient that is about 100-fold different for temperature compared to salinity.  $K_z$  is  
253 thus the same for all turbulent transport calculations no matter what gradient of what property.

254 For example, the vertical downgradient turbulent flux of dissolved iron transporting from iron-  
255 rich deeper waters upwards into the euphotic zone is computed as  $\frac{d}{dz} K_z d(\text{DFe})/dz$ .

256 According to Thorpe (1977), results from (1) and (2) are only useful after averaging over  
257 the size of a turbulent overturn instead of using single displacements. Here, root-mean-square  
258 rms-displacement values  $L_{\text{d}}$  are not determined over individual overturns, as in Dillon  
259 (1982), but over 7 m vertical intervals (equivalent to about 200 raw data samples) that just  
260 exceed average  $L_0$ . This avoids the complex distinction of smaller overturns in larger ones and  
261 allows the use of a single length scale of averaging. As a criterion for determining overturns we  
262 only used those data of which the absolute value of difference with the local reordered value  
263 exceeds a threshold of  $7 \times 10^{-5} \text{ kg m}^{-3}$ , which comes from standard deviations of the potential  
264 density profiles in near-homogeneous layers over 1-m intervals and which corresponds to noise-  
265 variational amplitudes applying a threshold of  $1.414 \times 10^{-4} \text{ kg m}^{-3}$  into raw data variations (e.g.,  
266 Galbraith and Kelley, 1996; Stansfield et al., 2001; Gargett and Garner, 2008). Vertically  
267 averaged turbulence values, short for averaged  $\epsilon$ - and  $K_z$ -values from (1) and (2), can be  
268 calculated to within an error of a factor of two to three, approximately. As will be demonstrated  
269 below, this is considerably less spread in values than the natural turbulence values variability  
270 over typically four orders of magnitude at a given position and depth in the ocean (e.g., Gregg,  
271 1989).

### 273 3 Results

#### 274 3.1 Physical parameters

275 An early morning vertical profile of density anomaly in the upper 500 m at a northern  
276 station (Fig. 3a) is characterized by a near-homogeneous layer of about 15 to 40 m, which is  
277 above a layer of relatively strong stratification and a smooth moderate stratification deeper  
278 below. In the near-homogeneous upper layer, in this example  $z > -30 \text{ m}$ , relatively large  
279 turbulent overturn displacements can be found of  $d = \pm 20 \text{ m}$  (Fig. 3b): so called large density

Formatted: Subscript

Formatted: Font color: Auto

281 inversions. In this paper we conventionally define ‘mixed layer depth’ as the depth at which the  
282 temperature difference with respect to the surface is 0.5°C (Jurado et al., 2012). We note that  
283 this actually more represents the ‘mixing layer depth’ and the reordered profile shows non-zero  
284 stratification. If the mixed-layer-depth definition would have been applying a temperature  
285 difference of, e.g., 0.001°C on the reordered profile, its value would average about 5 m, much  
286 less than using the present and more common, conventional definition applying a temperature  
287 difference of 0.5°C. We thus present turbulence results for this commonly defined ‘mixed layer’  
288 with caution, whilst observing their consistency with the results from deeper down, as presented  
289 below. For  $-200 < z < -30$  m, large turbulent overturns are few and far between. Turbulence  
290 dissipation rate (Fig. 3c) and eddy diffusivity (Fig. 3d) are characterized by relatively small  
291 displacement sizes of less than 5 m. For  $z < -200$  m, displacement values weakly increase with  
292 depth, together with stratification ( $\sim N^2$ ; Fig. 3e). Between  $-30 < z < 0$  m, turbulence dissipation  
293 rate values between our minimum detectable level  $< 10^{-11}$  and  $> 10^{-8} \text{ m}^2 \text{ s}^{-3}$  are similar to those  
294 found by others, using microstructure profilers (e.g., Oakey, 1982; Gregg, 1989), lowered  
295 acoustic Doppler current profiler or CTD-Thorpe scale analysis (e.g., Ferron et al., 1998; Walter  
296 et al., 2005; Kunze et al., 2006). Here, eddy diffusivities are found between our minimum  
297 detectable  $2 \times 10^{-5}$  and  $3 \times 10^{-3} \text{ m}^2 \text{ s}^{-1}$  and these values compare with previous near-surface  
298 results (Denman and Gargett, 1983). The relatively small  $|d| < 5$  m displacements (Fig. 3b) are  
299 genuine turbulent overturns, and they resemble ‘Rankine vortices’, a common model of  
300 cyclones (van Haren and Gostiaux, 2014), as may be best visible in this example in the large  
301 turbulent overturn near the surface. The occasional erratic appearance in individual profiles,  
302 sometimes still visible in the ten-profile means, reflects smaller overturns in larger ones.

303 A mid-morning profile at a southern station shows different characteristics (Fig. 4),  
304 although 500 m vertically averaged turbulence values are similar to within 10% of those of the  
305 northern station. This 10% variation is well within the error bounds of about a factor of two. At  
306 this southern station, the near-surface layer is stably stratifying (Fig. 4a) and displays few  
307 overturning displacements (Fig. 4b), while the interior demonstrates rarer but occasional

308 intense turbulent overturning (at  $z = -160$  m in Fig. 4), presumably due to internal wave  
309 breaking. At greater depths, stratification ( $\sim N^2$ ; Fig. 4e) weakly decreases, together with  $\epsilon$  (Fig.  
310 4c) and  $K_z$  (Fig. 4d).

311 Latitudinal overviews are given in Fig. 5 for: Average values over the upper  $z > -15$  m,  
312 which covers the diurnal mainly convective turbulent mixing range from the surface and under  
313 the cautionary note that these waters are weakly, but measurably stratified, average values  
314 between  $-100 < z < -25$  m, which covers the seasonal strong stratification, and average values  
315 between  $-500 < z < -100$  m, which covers the more permanent moderate stratification. Noting  
316 that all panels have a vertical axis representing a logarithmic scale, variations over nearly four  
317 orders of magnitude in turbulence dissipation rate (Fig. 5a) and eddy diffusivity (Fig. 5b) are  
318 observed between casts at the same station. This variation in magnitude is typically found in  
319 near-surface open-ocean turbulence microstructure profiles (e.g., Oakey, 1982). Still,  
320 considerable variability over about two orders of magnitude is observed between the averages  
321 from the different stations. This variation in station- and vertical averages far exceeds the  
322 instrumental error bounds of a factor of two (0.3 on a log-scale), and thus reveals local  
323 variability. The turbulence processes occur ‘intermittently’.

324 The observed variability over two orders of magnitude between yoyo-casts at a single  
325 station may be due to active convective overturning during early morning in the near-  
326 homogeneous upper layer, or due to internal wave breaking and sub-mesoscale variability  
327 deeper down. Despite the large variability at stations, trends are visible between stations in the  
328 upper 100 m over the  $332^\circ$  latitudinal range going poleward: Buoyancy frequency ( $\sim$  square  
329 root of stratification) steadily decreases significantly ( $p$ -value  $< 0.05$ ) given the spread of values  
330 at given stations, with the notion that near-surface ( $-15 < z < 0$  m) values show the same  
331 latitudinal trend as deeper-down-values across a larger spread of values, while turbulence  
332 values vary insignificantly with latitude as they remain the same or weakly increase by about  
333 half an order of magnitude (about a factor of 3). At a given depth range, turbulence dissipation  
334 rates roughly follow a log-normal distribution with standard deviations well exceeding half an  
335 order of magnitude. The comparison of latitudinal variations with the (log-normal) distribution

336 ~~isare~~ declared insignificant with  $p > 0.05$  when the mean values are found within 2 standard  
337 deviations (see Appendix A2). This is not only performed for turbulence dissipation rate, but  
338 also for other quantities. The trends suggest only marginally larger turbulence going poleward,  
339 which is possibly due to larger cooling from above and larger internal wave breaking deeper  
340 down. It is noted that the results are somewhat biased by the sampling scheme, which changed  
341 from 3 to 4 h after sunrise sampling at high latitudes to 4 to 5 h after sunrise sampling at lower  
342 latitudes, see the sampling hours after local sunrise in (Fig. 5d). Its effect is difficult to quantify,  
343 but should not show up in turbulence values from deeper down ( $-500 < z < -100$  m).

344 Between  $-500 < z < -100$  m, no clear significant trend with latitude is visible in the  
345 turbulence values (Fig. 5a,b), although  $[K_z]$  weakly increases with increasing latitude at all  
346 levels between  $-500 < z < 0$  m, while buoyancy frequency significantly decreases (Fig. 5c). The  
347 data from well-stratified waters deeper down thus show the same latitudinal trend as the  
348 observations from the near-surface layers. even though the latter are less well determined  
349 because of the weak stratification. Our turbulence values from CTD-data also confirm previous  
350 results by Jurado et al. (2012) who made microstructure profiler observations from the upper  $z$   
351  $> -100$  m along the same transect. Their results showed turbulence values remain unchanged  
352 over  $30^\circ$  latitude or increase by at most one order of magnitude, depending on depth level. Their  
353 'mixed' layer ( $z > \sim -25$  m) turbulence values are similar to our  $z > -15$  m values and half to one  
354 order of magnitude larger than the present deeper observations. The slight discrepancy in values  
355 averaged over  $z > -25$  m may point at either i) a low bias due to a too strict criterion of accepting  
356 density variations for reordering applied here, or ii) a high bias of the  $\sim 10$ -m largest overturns  
357 having similar velocity scales (of about  $0.05 \text{ m s}^{-1}$ ) as their  $0.1 \text{ m s}^{-1}$  slowly descending SCAMP  
358 microstructure profiler. At greater depths,  $-500 < z < -100$  m, it is seen in the present  
359 observations that the spread in turbulence values over four orders of magnitude at a particular  
360 station is also large. This spread in values suggests that dominant turbulence processes show  
361 similar intermittency in weakly (at high-latitudes  $N \approx 10^{-2.5} \text{ s}^{-1}$ ) and moderately (at mid-latitudes  
362  $N \approx 10^{-2.2} \text{ s}^{-1}$ ) stratified waters, respectively, for the given resolution of the instrumentation.

363 Mean values of N are larger by half an order of magnitude in the seasonal pycnocline (found  
364 in the range  $-100 < z < -25$  m) than those near the surface and in the more permanent  
365 stratification below (Fig. 5). Such local vertical variations in N have the same range of variation  
366 as observed horizontally across latitudes  $[30, 63]^\circ$  per depth level.

367

### 368 **3.2 Nutrient distributions and fluxes**

369 Vertical profiles of macro-nutrients generally resemble those of density anomaly in the  
370 upper  $z > -500$  m (Fig. 6). In the south, low macro-nutrient values are generally distributed over  
371 a somewhat larger near-surface mixed layer. The mixed layer depth, at which temperature  
372 differed bydefined as the depth at which the temperature difference with respect to the surface  
373 was  $0.5^\circ\text{C}$  from the surface (Jurado et al., 2012), varies between about 20 and 30 m on the  
374 southern end of the transect and weakly becomes shallower with latitude (Fig. 7a). This weak  
375 trend may be expected from the summertime wind conditions that also barely vary with latitude  
376 (Fig. 7b,c). In contrast, the euphotic zone, defined as the depth of the 0.1% irradiance  
377 penetration level (Mojica et al., 2015), demonstrates a clear latitudinal trend decreasing from  
378 about 150 to 50 m (Fig. 7a). For  $z < -100$  m below the seasonal stratification, vertical gradients  
379 of macro-nutrients are large (Fig. 6b-d). Macro-nutrient values become approximatelymoreor  
380 less independent of latitude at depths below  $z < -500$  m. Dissolved iron profiles differ from  
381 macro-nutrient profiles, notably in the upper layer near the surface (Fig. 6a). At some southern  
382 stations, dissolved iron and to a lesser extent also phosphate, have relatively high concentrations  
383 closest to the surface. These near-surface concentration increases suggest atmospheric sources,  
384 most likely Saharan dust deposition (e.g., Rijkenberg et al., 2012).

385 As a function of latitude in the near-surface ‘mixed’ layer (Fig. 8), the vertical turbulent  
386 fluxes of dissolved iron and phosphate (representing the macro-nutrients, for graphical reasons,  
387 see the similarity in profiles in Fig. 6b-d) are found constant or insignificantly ( $p > 0.05$ )  
388 increasing (Fig. 8d). Here, the mean eddy diffusivity values for the near-surface layer as  
389 presented in Fig. 5 are used for computing the fluxes. It is noted that in this layer turbulent  
390 overturning (Figs 3b, 4b) is larger and nutrients are mainly depleted (Fig. 6), except when

391 replenished from atmospheric sources in which case gradients reverse sign as in most DFe-  
392 profiles. Hereby, lateral diffusion is not considered important. Nonetheless, macro-nutrients are  
393 seen to increase significantly towards higher latitudes (Fig. 8b). We note that the vertical  
394 gradients in Fig. 8c, in which only downgradient values are plotted, are very weak in general  
395 within the standard deviation of measurements. The results in Fig. 8d are thus merely indicative,  
396 but they are consistent with the results from deeper down presented below.

397 More importantinterestingly, the significant vertical turbulent fluxes of nutrients across the  
398 seasonal pycnocline (Fig. 9) are found ambiguously or statistically independently varying with  
399 latitude (Fig. 9d). Likewise, the vertical turbulent fluxes of dissolved iron and phosphate are  
400 marginally constant with latitude across the more permanent stratification deeper down (Fig.  
401 10). Nitrate fluxes show the same latitudinal trend, with values around  $10^6$  mmol m<sup>-2</sup> s<sup>-1</sup>.  
402 Overall, the vertical turbulent nutrient fluxes across the seasonal and more permanent  
403 stratification resemble those of the physical vertical turbulent mass flux, which is equivalent to  
404 the distribution of turbulence dissipation rate and which is latitude-invariant (Fig. 5a).

405

#### 406 **4 Discussion**

407 Practically, the upright positioning CTD while using an adaptation consisting of a custom-  
408 made equal-surface inlet worked well to minimize ship-motion effects on variable flow-  
409 imposed temperature variations. This improved calculated turbulence values from CTD-  
410 observations in general and in near-homogeneous layers in particular. The indirect comparison  
411 with turbulence values determined from previous microstructure profiler observations along the  
412 same transect (Jurado et al., 2012) confirms the same trends, although occasionally turbulence  
413 values were lower (to one order of magnitude in the present study). This difference in values  
414 may be due to the time-lapse of 8 years between the observations, but more likely it is due to  
415 inaccuracies in one or both methods. It is noted that any ocean turbulence observations cannot  
416 be made better than to within a factor of two (Oakey, pers. comm.). In that respect, the standard  
417 CTD with the here presented adaptation is a cheaper solution than additional microstructure

418 profiler observations. Although the general understanding, mainly amongst modellers, is that  
419 the Thorpe length method overestimates diffusivity (e.g., Scotti, 2015; Mater and  
420 Venayagamoorthy, 2015), this view is not shared amongst ocean observers (e.g., Gregg et al.,  
421 2018). In the large parameter space of the high Reynolds number environment of the ocean,  
422 turbulence properties vary constantly, with an interminglement of convection and shear-  
423 induced turbulence at various levels. Given sufficient averaging, and adequate mean value  
424 parametrization, the Thorpe length method is not observed to overestimate diffusivity. This  
425 property of adequate and sufficient averaging yields similar mean parameter values in recent  
426 modelling results estimating a mixing coefficient near the classical bound of 0.2 in stationary  
427 flows for a wide range of conditions (Portwood et al., 2019). It is noted that diffusivity always  
428 requires knowledge of stratification to obtain a turbulent flux, and it is better to consider  
429 turbulence dissipation rate for intercomparison purposes. Nevertheless, future research may  
430 perform a more extensive comparison between Thorpe scale analysis data and deeper  
431 microstructure profiler data.

432 While our turbulence values are roughly similar to those of others transecting the NE-  
433 Atlantic over the entire water depth (Walter et al., 2005; Kunze et al., 2006), the focus in the  
434 present paper is on the upper 500 m because of its importance for upper-ocean marine biology.  
435 Our study demonstrates a significant decrease of stratification with increasing latitude and  
436 decreasing temperature that, however, does not lead to significant variation in turbulence values  
437 and vertical turbulent fluxes. Our direct estimates of the turbulent flux of nitrate into the  
438 euphotic zone are one to two orders of magnitude less than the previously estimated rate of  
439 nitrate uptake for the summer period within it for the same period. OurThe turbulent flux of  
440 nitrate values are of the same order of magnitude as reported by others (Cyr et al., 2015 and  
441 references therein). In particular, the Martin et al. (2010) study in the Northeast Atlantic Ocean  
442 (at 49°N, 16°W) reported similar vertical nutrient fluxes during summer, which provides  
443 confidence in the methods used. The same authors reported that the vertical nitrate flux into the  
444 euphotic zone was much lower than the rate of nitrate update at the time. To determine these  
445 nitrate uptake rates, they spiked water samples with a minimum of 0.5  $\mu\text{M}$  nitrate, representing

446 ~10% of the ambient nitrate concentration. In our study area, the ambient nitrate concentrations  
447 in the euphotic zone were much lower (see also Mojica et al., 2015), implying a higher relative  
448 importance of nitrate input to the overall uptake demand. Still, primary productivity in the  
449 oligotrophic euphotic zone, as well as in the high latitude Atlantic, is mainly fueled by recycling  
450 (e.g., Gaul et al., 1999; Achterberg et al., 2020) and the supply of new nutrients by turbulent  
451 fluxes, however small, provides a welcome addition. Besides nutrient input resulting from  
452 vertical turbulent fluxes, there is a role for latitudinal differences through the supply of nutrients  
453 by deep mixing events, and depending on the location, also potential upwelling and lateral  
454 transport events.

455 We suggest that internal waves may drive the feed-back mechanism, participating in the  
456 subtle balance between destabilizing shear and stable (re)stratification. Molecular diffusivity of  
457 heat is about  $10^{-7} \text{ m}^2 \text{ s}^{-1}$  in seawater, and nearly always smaller than turbulent diffusivity in the  
458 ocean. The average values of  $K_z$  during our study were typically 100 to 1000 times larger than  
459 molecular diffusivity, which implies turbulent diapycnal mixing drives vertical fluxes despite  
460 the relatively slow turbulence compared to surface wave breaking. Depending on the gradient  
461 of a substance like nutrients or matter, the relatively slow turbulence may not necessarily  
462 provide weak fluxes  $-K_z d(\text{substance})/dz$  into the photic zone. In the central North Sea, a  
463 relatively low mean value of  $K_z = 2 \times 10^{-5} \text{ m}^2 \text{ s}^{-1}$  comparable to values over the seasonal  
464 pycnocline here, was found sufficient to supply nutrients across the strong summer pycnocline  
465 to sustain the entire late-summer phytoplankton bloom in near-surface waters and to warm up  
466 the near-bottom waters by some  $3^\circ\text{C}$  over the period of seasonal stratification (van Haren et al.,  
467 1999). There, the turbulent exchange was driven by a combination of tidal currents modified  
468 by the stratification, shear by inertial motions driven by the Coriolis force (inertial shear) and  
469 internal wave breaking. Such drivers are also known to occur in the open ocean, although to an  
470 unknown extent.

471 The here observed (lack of) latitudinal trends of  $\epsilon$ ,  $K_z$  and  $N$  yield approximately more or  
472 less the same information as the vertical trends in these parameters at all stations. In the vertical  
473 for  $z < -200 \text{ m}$ , turbulence values of  $\epsilon$  and  $K_z$  weakly vary with stratification. This is perhaps

474 unexpected and contrary to the common belief of stratification hampering vertical turbulent  
475 exchange of matter including nutrients. It is less surprising when considering that increasing  
476 stratification is able to support larger shear. Known sources of destabilizing shear include near-  
477 inertial internal waves of which the vertical length-scale is relatively small compared to other  
478 internal waves, including internal tides (LeBlond and Mysak, 1978).

479 The dominance of inertial shear over shear by internal tidal motions (internal tide shear),  
480 together with larger energy in the internal tidal waves, has been observed in the open-ocean,  
481 e.g. in the Irminger Sea around 60°N (van Haren, 2007). The frequent atmospheric disturbances  
482 in that area generate inertial motions and dominant inertial shear. Internal tides have larger  
483 amplitudes but due to much larger length scales they generate weaker shear, than inertial  
484 motions. Small-scale internal waves near the buoyancy frequency are abundant and may break  
485 sparsely in the ocean interior outside regions of topographic influence. However, larger  
486 destabilizing shear requires larger stable stratification to attain a subtle balance of 'constant'  
487 marginal stability (van Haren et al., 1999). Not only storms, but allother geostrophic  
488 adjustments, such as frontal collapse, may generate inertial wave shear also at low latitudes  
489 (Alford and Gregg, 2001), so that overall latitudinal dependence may be negligible. If shear-  
490 induced turbulence in the upper ocean is dominant it may thus be latitudinally independent  
491 (shallow ob~~ers~~ervations by Jurado et al., 2012; deeper observations in present study). There are  
492 no indications that the overall open ocean internal wave field and (sub)mesoscale activities are  
493 energetically much different across the mid-latitudes. If internal tide sources would have  
494 dominated our observations, clear differences in turbulence dissipation rates would have been  
495 found at our station near 48 °N (near the Porcupine Bank), for example, compared with those  
496 at other stations.

497 Summarizing, our study infers that vertical nutrient fluxes did not vary significantly with  
498 latitude and stratification. This suggests that predicted changes in the physical environment due  
499 to global ocean warming have little effect on vertical turbulent exchange. Supposing that  
500 enhanced warming leads to more stable stratification, more internal waves can be supported  
501 (LeBlond and Mysak, 1978), which upon breaking can maintain the extent of vertical turbulent

502 exchange and thereby, for example, vertical nutrient fluxes. We thus hypothesize that, from a  
503 physical environment perspective, in stratified oligotrophic waters the nutrient input from  
504 deeper waters and corresponding summer phytoplankton productivity and growth are not  
505 expected to change (much) with future global warming. We invite future observations and  
506 numerical modelling to further investigate this suggestion and associated feed-back  
507 mechanisms such as internal wave breaking.

508

509 *Competing interests.* The authors declare that they have no conflict of interest.

510

511 *Acknowledgements.* We thank the master and crew of the R/V Pelagia for their pleasant  
512 contributions to the sea-operations. J. van Heerwaarden and R. Bakker made the CTD-  
513 modification. We much appreciated the critical comments of the reviewers.

514

515

## APPENDIX A1

516 **Modification of CTD pump-tubing to minimize RAM-effects**

517 The unique pump system on SeaBird Electronics (SBE) CTDs, foremost on their high-  
518 precision full ocean depth shipborne and cable-lowered SBE911, minimizes the effects of flow  
519 variations (and inversions) past its T-C sensors (SeaBird, 2012). This reduction in flow  
520 variation is important, because the T-sensor has a slower response than the C-sensor. As data  
521 from the latter are highly temperature dependent, besides being pressure dependent, the precise  
522 matching of all three sensors is crucial for establishing proper salinity and density  
523 measurements, especially across rapid changes in any of the parameters. As flow past the T-  
524 sensor causes higher measurement values due to friction at the sensor tip, flow-fluctuations are  
525 to be avoided as they create artificial T-variations of about  $1 \text{ mK s m}^{-1}$  (Larson and Pedersen,  
526 1996).

527 However, while the pump itself is one thing, its tubing needs careful mounting as well, with  
528 in- and outlet at the same depth level (Sea-Bird, 2012). This is to prevent ram pressure  $P = \rho U^2$ ,  
529 for density  $\rho$  and flow speed  $U$ . Unfortunately, the SBE-manual shows tubing of different  
530 diameters, for in- and outlet. Different diameter tubing leads to velocity fluctuations of  $\pm 0.5 \text{ m}$   
531  $\text{s}^{-1}$  past the T-sensor, as was concluded from a simple experiment by van Haren and Laan  
532 (2016). The flow speed variations induce temperature variations of  $\pm 0.5 \text{ mK}$  and are mainly  
533 detectable in weakly stratified waters such as in the deep ocean, but also near the surface as  
534 observed in the present data. Using tubes of the same diameter opening remedied most of the  
535 effect, but only if the surface of the tube-opening is perpendicular to the main CT-motion as in  
536 a vertically mounted CTD. If it is parallel to the main motion as in a horizontally mounted CTD,  
537 the effect was found to be adverse. The make-shift onboard experiment in van Haren and Laan  
538 (2016) has now been cast into a better design (Fig. A1), of which the first results are presented  
539 in this paper.

540

## APPENDIX A2

541 **PDFs of vertically averaged dissipation rate in comparison with latitudinal trends**

542 Ocean turbulence dissipation rate generally tends to a nearly log-normal distribution (e.g.,  
543 Pearson and Fox-Kemper, 2018), so that the probability density function (PDF) of the logarithm  
544 of  $\varepsilon$ -values is normally distributed and can be described by the first two moments, the mean  
545 and its standard deviation. It is seen in Fig. A2a that the overall distribution of all present data  
546 indeed approaches lognormality, despite the relatively large length-scale used in the  
547 computations (cf., Yamazaki and Lueck, 1990). When the data are split into the three depth  
548 levels as in Fig. 5a, it is seen that  $\varepsilon$  in the upper  $z > -15$  m layer is not log-normally distributed  
549 due to a few outlying high values confirming an ocean state dominated by a few turbulence  
550 bursts (Moum and Rippeth, 2009), whereas  $\varepsilon$  in the deeper more stratified layers is nearly log-  
551 normally distributed.

552 When we compare the mean and standard deviations of the distributions with the extreme  
553 values of the latitudinal trends as computed for Fig. 5a it is seen that for none of the three depth  
554 levels the extreme values are found outside one standard deviation from the mean value. In fact,  
555 for deeper stratified waters the extreme values of the trends are found very close to the mean  
556 value. It is concluded that the mean dissipation rate does not show a significant trend with  
557 latitude, at all depth levels. The same exercise yields extreme buoyancy frequency values lying  
558 outside one standard deviation from the mean values for well-stratified waters, from which we  
559 conclude that stratification significantly decreases with latitude. This is inferable from Fig. 5c  
560 by investigating the spread of mean values around the trend line.

561

562 **References**

563 Alford, M. H. and Gregg, M. C.: Near-inertial mixing: Modulation of shear, strain and  
564 microstructure at low latitude, *J. Geophys. Res.*, 106, 16,947-16,968, 2001.

565 Achterberg, E. P.: Trace element biogeochemistry in the high latitude North Atlantic Ocean:  
566 seasonal variations and volcanic inputs, *Glob. Biogeochem. Cycl.*.. in press, doi:  
567 10.1029/2020GB006674, 2020.

568 Charria, G., Theetten, S., Vandermeirsch, F., Yelekçi, Ö and Audiffren, N.: Interannual  
569 evolution of (sub)mesoscale dynamics in the Bay of Biscay, *Ocean Sci.*, 13, 777-797, 2017.

570 Cyr, F., Bourgault, D., Galbraith, P. S. and Gosselin, M.: Turbulent nitrate fluxes in the Lower  
571 St. Lawrence Estuary, Canada, *J. Geophys. Res.*, 120, 2308-2330,  
572 doi:10.1002/2014JC010272, 2015.

573 De Baar, H. J. W. et al.: Titan: A new facility for ultraclean sampling of trace elements and  
574 isotopes in the deep oceans in the international Geotraces program, *Mar. Chem.*, 111, 4-21,  
575 2008.

576 Denman, K. L. and Gargett, A. E.: Time and space scales of vertical mixing and advection of  
577 phytoplankton in the upper ocean, *Limnol. Oceanogr.*, 28, 801-815, 1983.

578 Dillon, T. M.: Vertical overturns: A comparison of Thorpe and Ozmidov length scales, *J.*  
579 *Geophys. Res.*, 87, 9601-9613, 1982.

580 Ferron, B., Mercier, H., Speer, K., Gargett, A. and Polzin, K.: Mixing in the Romanche Fracture  
581 Zone, *J. Phys. Oceanogr.*, 28, 1929-1945, 1998.

582 Galbraith, P. S. and Kelley, D. E.: Identifying overturns in CTD profiles, *J. Atmos. Oc.*  
583 *Technol.*, 13, 688-702, 1996.

584 Gargett, A. and Garner, T.: Determining Thorpe scales from ship-lowered CTD density  
585 profiles, *J. Atmos. Oc. Technol.*, 25, 1657-1670, 2008.

586 Gaul, W., Antia, A. N. and Koeve, W.: Microzooplankton grazing and nitrogen supply of  
587 phytoplankton growth in the temperate and subtropical northeast Atlantic, *Mar. Ecol. Progr.*  
588 *Ser.*, 189, 93-104, 1999.

589 Gill, A. E.: *Atmosphere-Ocean Dynamics*, Academic Press, Orlando, Fl, USA, 662 pp, 1982.

590 Grasshoff, K., Kremling, K. and Ehrhardt, M.: Methods of seawater analysis, Verlag  
591 Chemie GmbH, Weinheim, 419 pp, 1983.

592 Gregg, M. C.: Scaling turbulent dissipation in the thermocline, *J. Geophys. Res.*, 94, 9686-  
593 9698, 1989.

594 Gregg, M. C., Sanford, T. B. and Winkel, D. P.: Reduced mixing from the breaking of internal  
595 waves in equatorial waters, *Nature*, 422, 513-515, 2003.

596 Gregg, M. C., D'Asaro, E. A., Riley, J. J. and Kunze, E.: Mixing efficiency in the ocean, *Ann.*  
597 *Rev. Mar. Sci.*, 10, 443-473, 2018.

598 Henyey, F. S., Wright, J. and Flatte, S. M.: Energy and action flow through the internal wave  
599 field - an eikonal approach, *J. Geophys. Res.*, 91, 8487-8495, 1986.

600 Hernández-Hernández, N. et al.: Drivers of plankton distribution across mesoscale eddies at  
601 submesoscale range, *Front. Mar. Sci.*, 7, 667, doi:10.3389/fmars.2020.00667, 2020.

602 Hibiya T., Nagasawa, M. and Niwa, Y.: Latitudinal dependence of diapycnal diffusivity in the  
603 thermocline observed using a microstructure profiler, *Geophys. Res. Lett.*, 34, L24602,  
604 2007.

605 Huisman, J., Pham Thi, N. N., Karl, D. M. and Sommeijer, B.: Reduced mixing generates  
606 oscillations and chaos in the oceanic deep chlorophyll maximum, *Nature*, 439, 322-325,  
607 2006.

608 Jurado, E., van der Woerd, H. J. and Dijkstra, H. A.: Microstructure measurements along a  
609 quasi-meridional transect in the northeastern Atlantic Ocean, *J. Geophys. Res.*, 117,  
610 C04016, doi:10.1029/2011JC07137, 2012.

611 IOC, SCOR, IAPSO: The international thermodynamic equation of seawater – 2010:  
612 Calculation and use of thermodynamic properties, Intergovernmental Oceanographic  
613 Commission, Manuals and Guides No. 56, UNESCO, Paris, France, 196 pp, 2010.

614 Johnson, K. S., Gordon, R. M. and Coale, K. H.: What controls dissolved iron concentrations  
615 in the world ocean? *Mar. Chem.*, 57, 137-161, 1997.

616 King, B. et al.: Buoyancy frequency profiles and internal semidiurnal tide turning depths in the  
617 oceans, *J. Geophys. Res.*, 117, C04008, 2012, doi:10.1029/2011JC007681.

618 Klunder, M. B., Laan, P., Middag, R., De Baar, H. J. W. and van Ooijen, J. C.: Dissolved iron  
619 in the Southern Ocean (Atlantic sector), *Deep-Sea Res. II*, 58, 2678-2694, 2011.

620 Kunze, E., Firing, E., Hummon, J. M., Chereskin, T. K. and Thurnherr, A. M.: Global  
621 abyssal mixing inferred from lowered ADCP shear and CTD strain profiles, *J. Phys.*  
622 *Oceanogr.* 36, 1553-1576, 2006.

623 Larson, N., Pedersen, A. M.: Temperature measurements in flowing water: viscous heating  
624 of sensor tips, Proc. 1st IGHEM Meeting, Montreal, PQ, Canada. [Available online at  
625 [http://www.seabird.com/technical\\_references/viscous.htm](http://www.seabird.com/technical_references/viscous.htm)], 1996.

626 LeBlond, P. H. and Mysak, L. A.: Waves in the Ocean, Elsevier, Amsterdam NL, 602 pp, 1978.

627 Lueck, R. G.: Thermal inertia of conductivity cells: Theory, *J. Atmos. Oc. Technol.*, 7, 741-  
628 755, 1990.

629 Mater, B. D., Venayagamoorthy, S. K., St. Laurent, L. and Moum, J. N.: Biases in Thorpe-scale  
630 estimates of turbulence dissipation. Part I: Assessments from largescale overturns in  
631 oceanographic data, *J. Phys. Oceanogr.*, 45, 2497-2521, 2015.

632 Martin A. P., et al.: The supply of nutrients due to vertical turbulent mixing: A study at the  
633 Porcupine abyssal plain study site in the northeast Atlantic, *Deep-Sea Res. II*, 57, 1293-  
634 1302, 2010.

635 Mensah, V., Le Menn, M. and Morel, Y.: Thermal mass correction for the evaluation of salinity,  
636 *J. Atmos. Oc. Tech.*, 26, 665-672, 2009.

637 Middag, R., de Baar, H. J. W., Laan, P. and Bakker, K.: Dissolved aluminium and the silicon  
638 cycle in the Arctic Ocean, *Marine Chemistry*, 115, 176-195, 2009.

639 Mojica, K. D. A. et al.: Phytoplankton community structure in relation to vertical stratification  
640 along a north-south gradient in the Northeast Atlantic Ocean, *Limnol. Oceanogr.*, 60, 1498-  
641 1521, 2015.

642 Mojica, K. D. A., Huisman, J., Wilhelm, S. W. and Brussaard, C. P. D.: Latitudinal variation  
643 in virus-induced mortality of phytoplankton across the North Atlantic Ocean, *ISME J.*, 10,  
644 500-513, 2016.

645 Moum, J. N. and Rippeth, T. P.: Do observations adequately resolve the natural variability of  
646 oceanic turbulence?, *J. Mar. Sys.*, 77, 409-417, 2009.

647 Murphy, J. and Riley, J. P.: A modified single solution method for the determination of  
648 phosphate in natural waters, *Anal. Chim. Acta*, 27, 31-36, 1962.

649 Oakey, N. S.: Determination of the rate of dissipation of turbulent energy from simultaneous  
650 temperature and velocity shear microstructure measurements, *J. Phys. Oceanogr.*, 12, 256-  
651 271, 1982.

652 Osborn, T. R.: Estimates of the local rate of vertical diffusion from dissipation measurements,  
653 *J. Phys. Oceanogr.*, 10, 83-89, 1980.

654 Pearson, B. and Fox-Kemper, B.: Log-normal turbulence dissipation in global ocean models,  
655 *Phys. Rev. Lett.*, 120, 094501, 2018.

656 Portwood, G. D., de Bruyn Kops, S. M. and Caulfield, C. P.: Asymptotic dynamics of high  
657 dynamic range stratified turbulence, *Phys. Rev. Lett.*, 122, 194504, 2019.

658 Rijkenberg, M. J. A. et al.: Fluxes and distribution of dissolved iron in the eastern (sub-) tropical  
659 North Atlantic Ocean, *Glob. Biogeochem. Cycl.*, 26, GB3004,  
660 doi:10.1029/2011GB004264, 2012.

661 Rijkenberg, M. J. A. et al.: "PRISTINE", a new high volume sampler for ultraclean sampling  
662 of trace metals and isotopes, *Mar. Chem.*, 177, 501-509, 2015.

663 Sarmiento, J. L. et al.: Response of ocean ecosystems to climate warming, *Glob. Biogeochem.*  
664 *Cycl.*, 18, doi:10.1029/2003GB002134, 2004.

665 Scotti, A.: Biases in Thorpe-scale estimates of turbulence dissipation. Part II: energetics  
666 arguments and turbulence simulations, *J. Phys. Oceanogr.*, 45, 2522-2543, 2015.

667 Sea-Bird: Fundamentals of the TC duct and pump-controlled flow used on Sea-Bird CTDs,  
668 *Proc. Sea-Bird Electronics Appl.* note 38, SBE, Bellevue, WA, USA, 5 pp, 2012.

669 Smith, W. H. F. and Sandwell, D. T. : Global seafloor topography from satellite altimetry and  
670 ship depth soundings, *Science* 277, 1957-1962, 1997.

671 Stansfield, K., Garrett, C., Dewey, R.: The probability distribution of the Thorpe displacement  
672 within overturns in Juan de Fuca Strait, *J. Phys. Oceanogr.*, 31, 3421-3434, 2001.

673 Strickland, J. D. H. and Parsons, T. R.: A practical handbook of seawater analysis, First  
674 edition, Fisheries Research Board of Canada, *Bulletin*, 167, 293 pp, 1968.

675 Thorpe, S. A.: Turbulence and mixing in a Scottish loch, *Phil. Trans. Roy. Soc. Lond. A*, 286,  
676 125-181, 1977.

677 van Haren, H.: Tidal and near-inertial peak variations around the diurnal critical latitude,  
678 *Geophys. Res. Lett.*, 32, L23611, doi:10.1029/2005GL024160, 2005.

679 van Haren, H.: Inertial and tidal shear variability above Reykjanes Ridge, *Deep-Sea Res. I*, 54,  
680 856-870, 2007.

681 van Haren, H. and Gostiaux, L.: Characterizing turbulent overturns in CTD-data, *Dyn. Atmos.*  
682 *Oc.*, 66, 58-76, 2014.

683 van Haren, H. and Laan, M.: An in-situ experiment identifying flow effects on temperature  
684 measurements using a pumped CTD in weakly stratified waters, *Deep-Sea Res. I*, 111, 11-  
685 15, 2016.

686 van Haren, H., Maas, L., Zimmerman, J. T. F., Ridderinkhof, H. and Malschaert, H.: Strong  
687 inertial currents and marginal internal wave stability in the central North Sea, *Geophys.*  
688 *Res. Lett.*, 26, 2993-2996, 1999.

689 Walter, M., Mertens, C. and Rhein, M.: Mixing estimates from a large-scale hydrographic  
690 survey in the North Atlantic, *Geophys. Res. Lett.*, 32, L13605, doi:10.1029/2005GL022471,  
691 2005.

692 Yamazaki, H. and Lueck, R.: Why oceanic dissipation rates are not lognormal, *J. Phys.*  
693 *Oceanogr.*, 20, 1907-1918, 1990.

694

695

696 **Figure 1.** Bathymetry map of the Northeast Atlantic Ocean based on the 9.1 ETOPO-1 version  
697 of satellite altimetry-derived data by Smith and Sandwell (1997). The numbered circles  
698 indicate the CTD stations, [at station 17 \(x\) no turbulence parameter, only nutrient sampling](#)  
699 [was done. At stations 1 and 2 no DFe-samples were taken, at station 18 no nutrient-samples](#)  
700 [were taken](#). Depth contours are at 2500 and 5000 m.

701  
702 **Figure 2.** Test of effective removal of ship motions in CTD-data after pump in- and outlet  
703 modification. Nearly raw 24 Hz sampled downcast data obtained from northern station 32  
704 (cast 9). Short example time series for the 20-m depth range [10, 30] m. (a) Detrended  
705 pressure (blue) and its (negative signed) first time derivative  $-dp/dt$ , 2-dbar-smoothed  
706 (purple). (b) Detrended temperature. (c) Moderately smoothed ( $\sim 30$  degrees of freedom;  
707 dof) spectra of data from the 5 to 500 m depth range. (d) Moderately smoothed (40 dof)  
708 coherence between  $dp/dt$  and T from c., with dashed line indicating the 95% significance  
709 level. (e) Corresponding phase difference.

710  
711 **Figure 3.** Upper 500 m of turbulence characteristics computed from downcast density anomaly  
712 data applying a threshold of  $7 \times 10^{-5} \text{ kg m}^{-3}$ . Northern station 29, cast 2. (a) Unordered, ‘raw’  
713 profile of density anomaly referenced to the surface. (b) Overturn displacements following  
714 reordering of the profiles in a. Slopes  $\frac{1}{2}$  (solid lines) and 1 (dashed lines) are indicated. (c)  
715 Logarithm of dissipation rate computed from the profiles in a., [r.m.s. calculated averaged](#)  
716 over 7 m intervals. [We use the mathematics expression ‘lg’ for the 10-base logarithm, as](#)  
717 [given in the ISO 80000 specification.](#) (d) As c., but for eddy diffusivity. (e) Logarithm of  
718 buoyancy frequency computed after reordering the profiles of a.

719  
720 **Figure 4.** As Fig. 3, but for a southern station. Upper 500 m of turbulence characteristics  
721 computed from downcast density anomaly data applying a threshold of  $7 \times 10^{-5} \text{ kg m}^{-3}$ .  
722 Southern station 3, cast 4. (a) Unordered, ‘raw’ profile of density anomaly referenced to  
723 the surface. (b) Overturn displacements following reordering of the profiles in a. Slopes  $\frac{1}{2}$

724 (solid lines) and 1 (dashed lines) are indicated. (c) Logarithm of dissipation rate computed  
725 from the profiles in a., r.m.s. calculated averaged over 7 m intervals. (d) As c., but for eddy  
726 diffusivity. (e) Logarithm of buoyancy frequency computed after reordering the profiles of  
727 a.

728  
729 **Figure 5.** Summer 2017 latitudinal transect along  $17 \pm 5^\circ\text{W}$  of turbulence values for upper 15 m  
730 averages (green) and averages between  $-100 < z < -25$  m (blue, seasonal pycnocline) and  
731  $-500 < z < -100$  m (black, more permanent pycnocline) from short yoyos of 3 to 6 CTD-  
732 casts. Values are given per cast (o) and station average (heavy circle with x; the size  
733 corresponds with  $\pm$ the standard error for turbulence parameters). (a) Logarithm of  
734 dissipation rate. (b) Logarithm of diffusivity. (c) Logarithm of buoyancy frequency (the  
735 small symbols have the size of  $\pm$ the standard error). (d) Hour of sampling after sunrise.

736  
737 **Figure 6.** Upper 500 m profiles for stations at three latitudes. (a) Density anomaly referenced  
738 to the surface, including profiles from Fig. 3a and 4a. (b) Nitrate plus nitrite. (c) Phosphate.  
739 (d) Silicate. (e) Dissolved iron.

740  
741 **Figure 7.** Latitudinal transect of near-surface layers and wind conditions measured at stations  
742 during the observational survey. (a) Mixed layer depth (x) and euphotic zone (o). (b) Wind  
743 speed. (c) Wind direction.

744  
745 **Figure 8.** Latitudinal transect of near-surface nutrient concentrations. (a) Dissolved iron  
746 measured at depths indicated. Missing values reflect not all depths were sampled. -(b)  
747 Nitrate plus nitrite (red) and phosphate (blue, scale times 10) measured at depths indicated  
748 in a. (c) Logarithm of very weak within standard deviations of measurements vertical  
749 gradients of values dissolved iron in a. (o-red) and phosphate in b. (x-blue). Only  
750 downgradient values are shown, which excludes several PO<sub>4</sub><sup>3-</sup> and nearly all DFe-gradient - - - { Formatted: Subscript  
751 values due to near-surface increased values (cf. Fig. 6e, 32°N profile) - (d) Upward - - - { Formatted: Font: Italic

752 **v**ertical turbulent fluxes of phosphate concentration gradients in c. using average surface  
753  $K_z$  from Fig. 5b, valid for depth average (here,  $\sim 17$  m) of depths in a.

754

755 **Figure 9.** As Fig. 8, but for  $-100 < z < -25$  m, with fluxes for  $\sim 62$  m in d.

756

757 **Figure 10.** As Fig. 8, but for  $-600$  (few nutrients sampled at 500)  $< z < -100$  m, with fluxes for  
758  $\sim 350$  m in d.

759

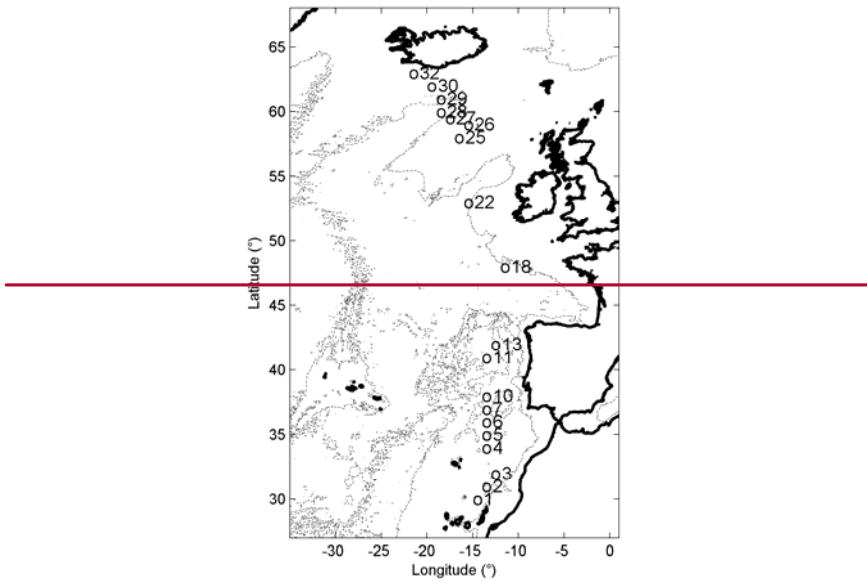
760 **Fig. A1.** SBE911 CTD-pump in- and outlet modification following the findings in van Haren  
761 and Laan (2016). (a) The T- and C-sensors clamped together with a structure holding in-  
762 and outlet pump-tubing of exactly the same diameter, separated at 0.3 m distance in the  
763 horizontal plane. (b) The modification of a. mounted in the CTD-frame.

764

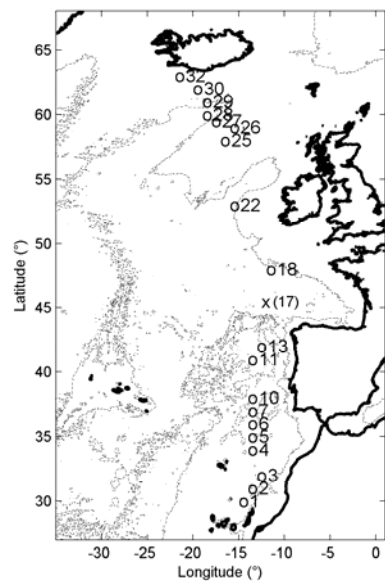
765 **Fig. A2.** Probability Density Functions of logarithm of vertically averaged dissipation rate in  
766 comparison with latitudinal trend extreme values. (a) Distribution as a function of latitude  
767 for all data. (b) As a, but for the upper 15 m averages only. The mean value is given by the  
768 vertical purple line, with the horizontal line indicating  $\pm 1$  standard deviation. The vertical  
769 light-blue lines indicate the best-fit value of the trend for  $30^\circ$  and  $63^\circ\text{N}$ . (c) As b, but for  
770 averages between  $-100 < z < -25$  m. (d) As c, but for averages between  $-500 < z < -100$  m.

771

772



773



774

775

776

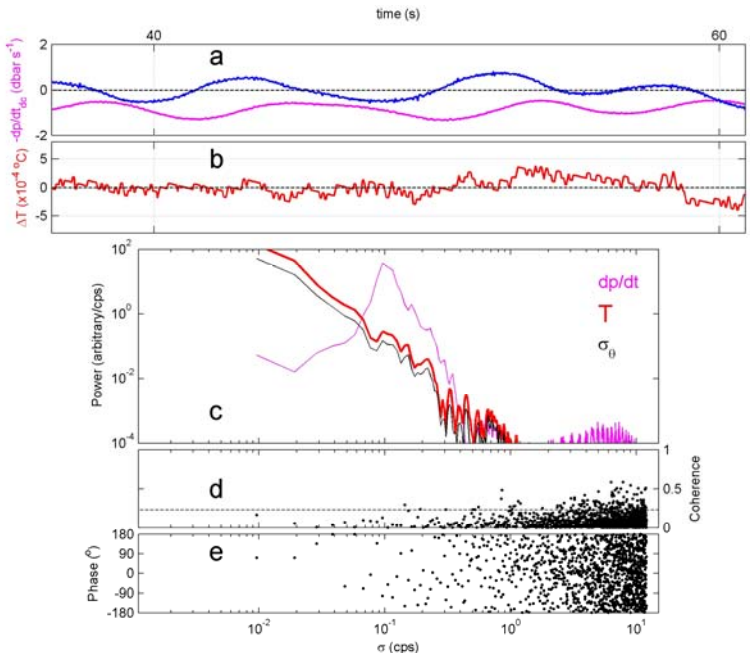
777

778

779

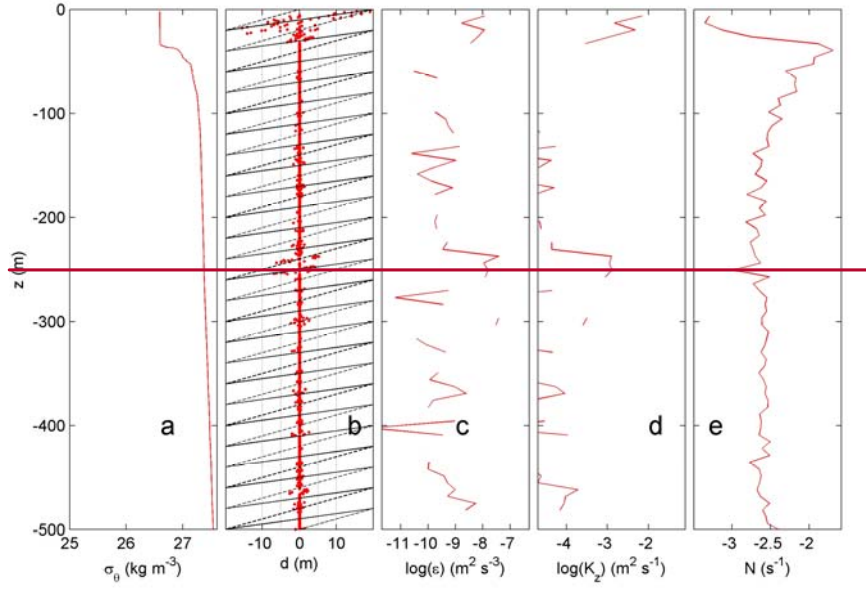
**Figure 1.** Bathymetry map of the Northeast Atlantic Ocean based on the 9.1 ETOPO-1 version of satellite altimetry-derived data by Smith and Sandwell (1997). The numbered circles indicate the CTD stations. at station 17 (x) no turbulence parameter, only nutrient sampling was done. At stations 1 and 2 no DFe-samples were taken, at station 18 no nutrient-samples were taken. Depth contours are at 2500 and 5000 m.





782  
 783 **Figure 2.** Test of effective removal of ship motions in CTD-data after pump in- and outlet  
 784 modification. Nearly raw 24 Hz sampled downcast data obtained from northern station 32  
 785 (cast 9). Short example time series for the 20-m depth range [10, 30] m. (a) Detrended  
 786 pressure (blue) and its (negative signed) first time derivative  $-dp/dt$ , 2-dbar-smoothed  
 787 (purple). (b) Detrended temperature. (c) Moderately smoothed (~30 degrees of freedom;  
 788 dof) spectra of data from the 5 to 500 m depth range. (d) Moderately smoothed (40 dof)  
 789 coherence between  $dp/dt$  and  $T$  from c., with dashed line indicating the 95% significance  
 790 level. (e) Corresponding phase difference.  
 791

792



793

794

795

796

797

798

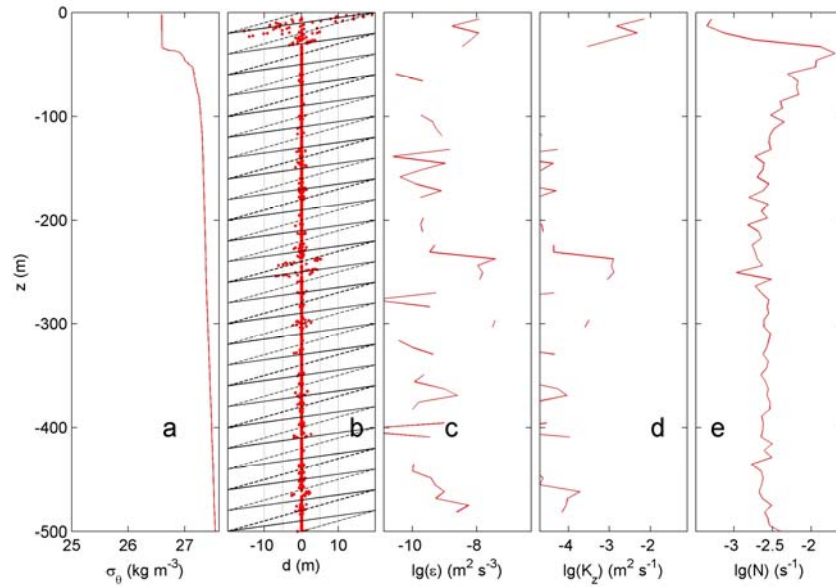
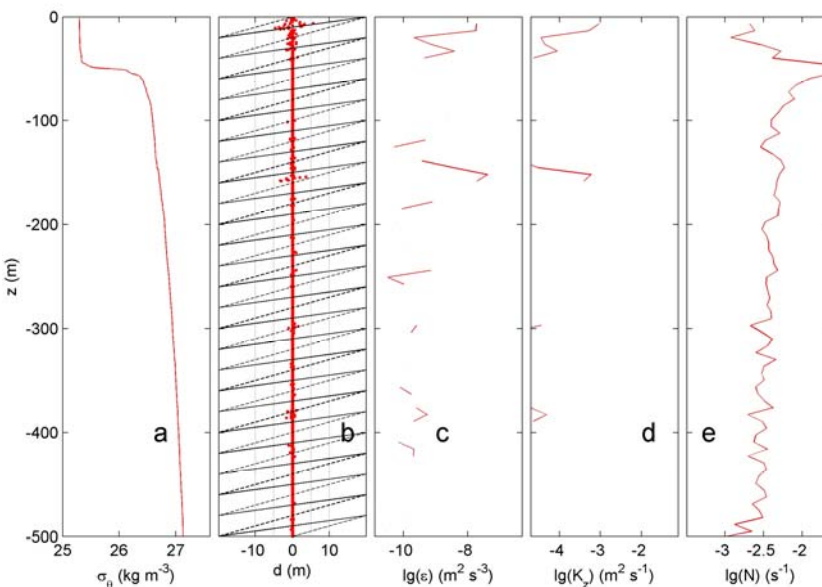
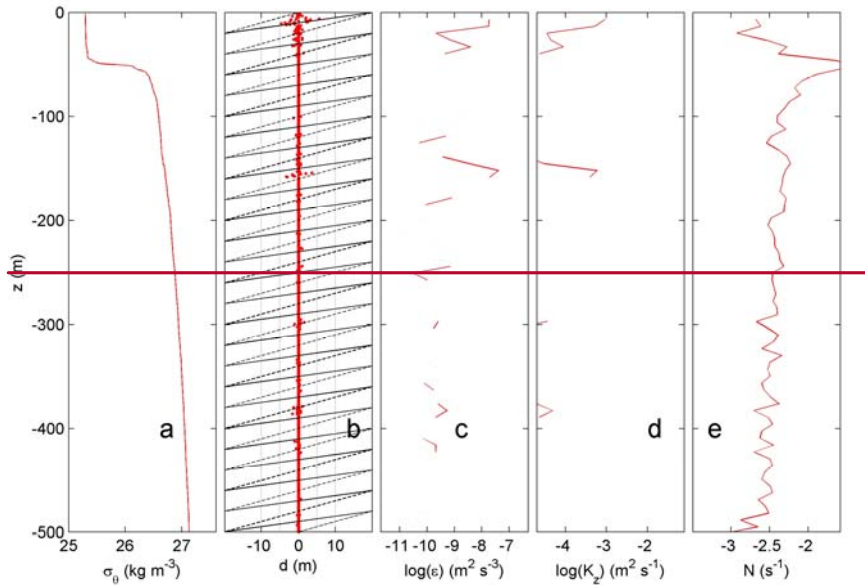


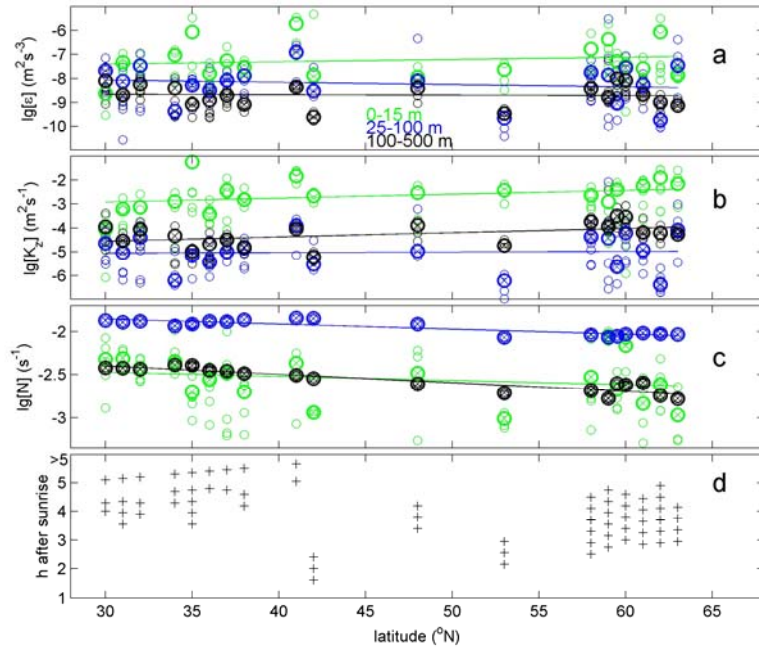
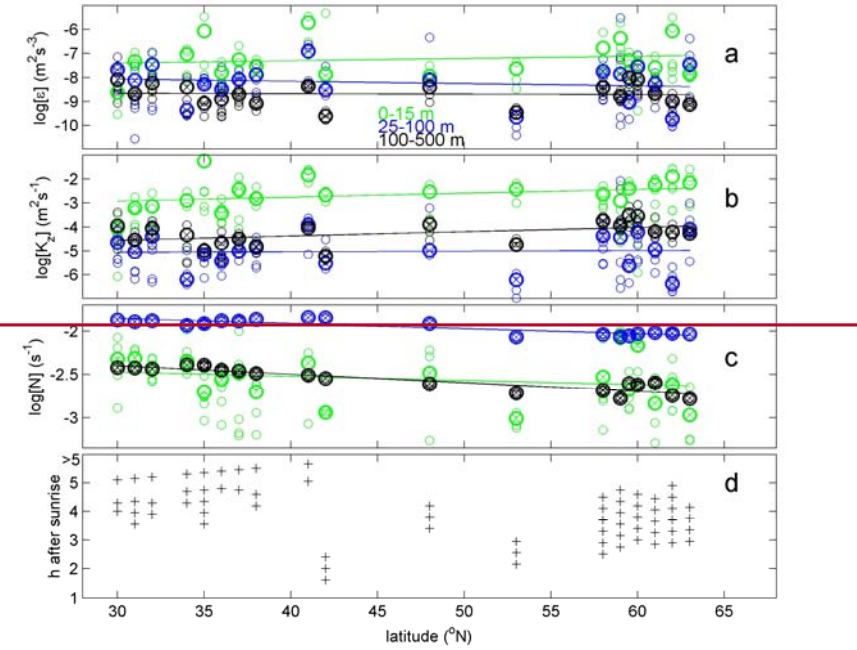
**Figure 3.** Upper 500 m of turbulence characteristics computed from downcast density anomaly data applying a threshold of  $7 \times 10^{-5} \text{ kg m}^{-3}$ . Northern station 29, cast 2. (a) Unordered, 'raw' profile of density anomaly referenced to the surface. (b) Overturn displacements following reordering of the profiles in a. Slopes  $1/2$  (solid lines) and  $1$  (dashed lines) are indicated. (c) Logarithm of dissipation rate computed from the profiles

799 in a., r.m.s. calculated averaged over 7 m intervals. We use the mathematics expression  
800 'lg' for the 10-base logarithm, as given in the ISO 80000 specification. (d) As c., but for  
801 eddy diffusivity. (e) Logarithm of buoyancy frequency computed after reordering the  
802 profiles of a.  
803



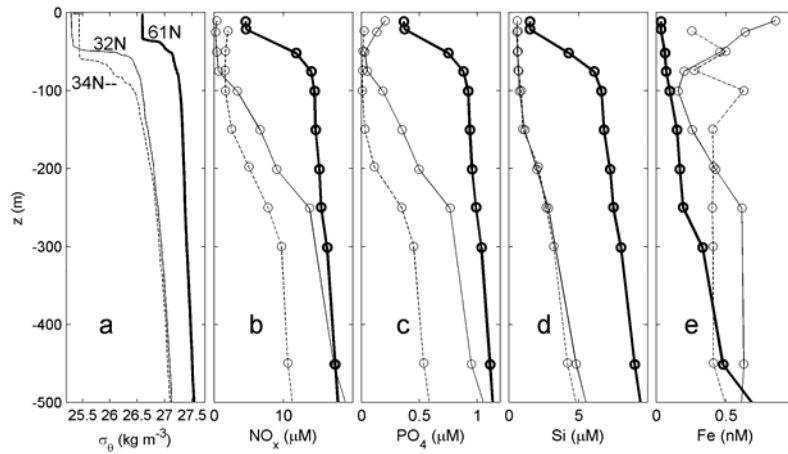
806  
807  
808  
809  
810  
811  
812  
813  
814

**Figure 4.** As Fig. 3, but for a southern station. Upper 500 m of turbulence characteristics  
computed from downcast density anomaly data applying a threshold of  $7 \times 10^{-5} \text{ kg m}^{-3}$ .  
Southern station 3, cast 4. (a) Unordered, ‘raw’ profile of density anomaly referenced to  
the surface. (b) Overturn displacements following reordering of the profiles in a. Slopes  $\frac{1}{2}$   
(solid lines) and 1 (dashed lines) are indicated. (c) Logarithm of dissipation rate computed  
from the profiles in a., r.m.s. calculated averaged over 7 m intervals. (d) As c., but for eddy  
diffusivity. (e) Logarithm of buoyancy frequency computed after reordering the profiles of  
a.



817 **Figure 5.** Summer 2017 latitudinal transect along  $17 \pm 5^\circ\text{W}$  of turbulence values for upper  
 818 15 m averages (green) and averages between  $-100 < z < -25$  m (blue, seasonal pycnocline)  
 819 and  $-500 < z < -100$  m (black, more permanent pycnocline) from short yoyos of 3 to 6  
 820 CTD-casts. Values are given per cast (o) and station average (heavy circle with x; the size  
 821 corresponds with  $\pm$ the standard error for turbulence parameters). (a) Logarithm of

822 dissipation rate. (b) Logarithm of diffusivity. (c) Logarithm of buoyancy frequency (the  
823 small symbols have the size of  $\pm$ the standard error). (d) Hour of sampling after sunrise.  
824



825  
826 **Figure 6.** Upper 500 m profiles for stations at three latitudes. (a) Density anomaly  
827 referenced to the surface, including profiles from Fig. 3a and 4a. (b) Nitrate plus nitrite. (c)  
828 Phosphate. (d) Silicate. (e) Dissolved iron.  
829

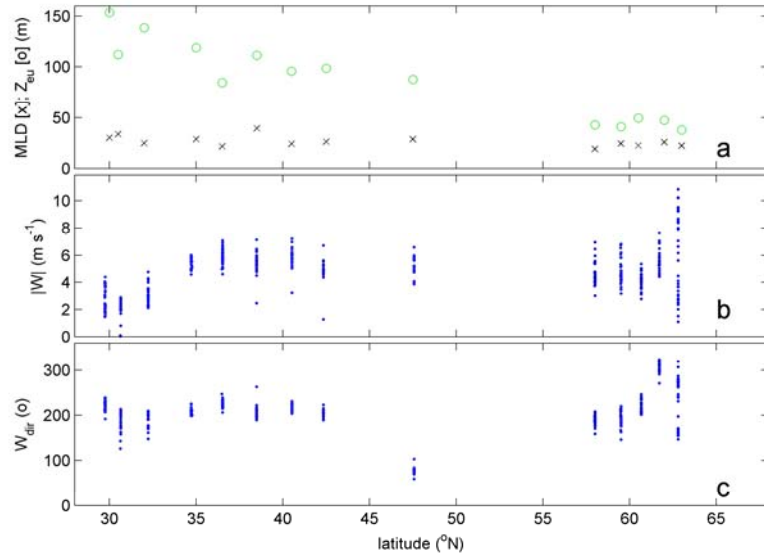


**Figure 7.** Latitudinal transect of near-surface layers and wind conditions measured at stations during the observational survey. (a) Mixed layer depth (x) and euphotic zone (o). (b) Wind speed. (c) Wind direction.

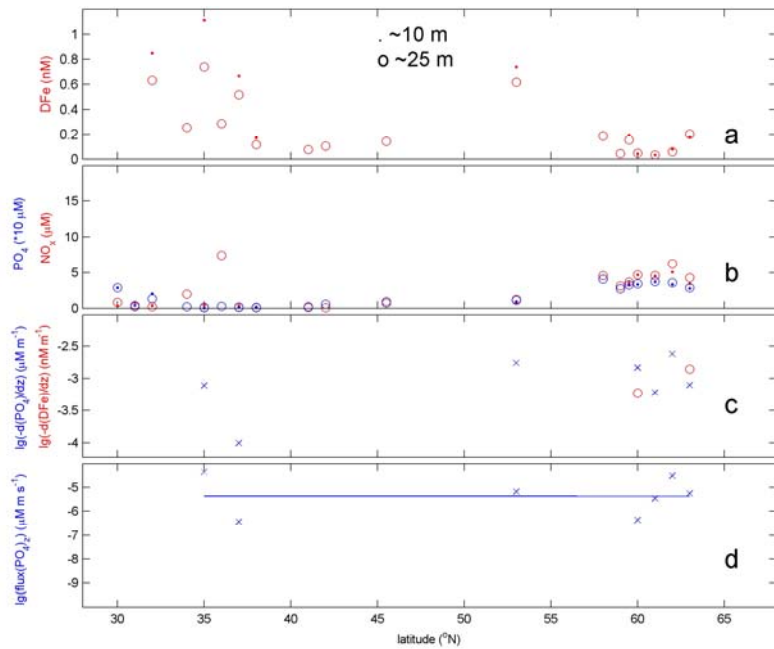
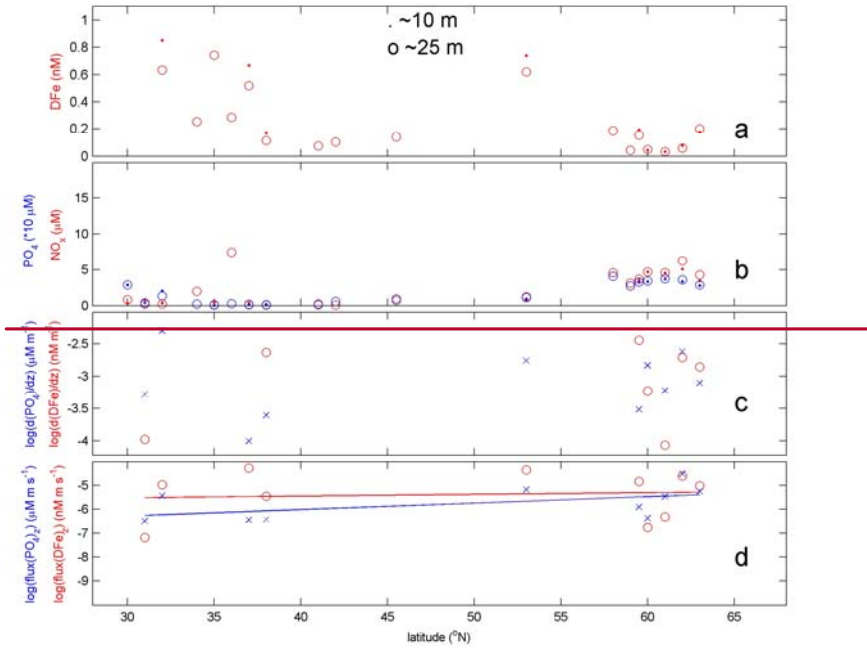


**Figure 8.** Latitudinal transect of near-surface nutrient concentrations. (a) Dissolved iron measured at depths indicated. *Missing values reflect not all depths were sampled.* (b) Nitrate plus nitrite (red) and phosphate (blue, scale times 10) measured at the depths indicated in a. (c) Logarithm of *(very weak within standard deviations of measurements)* vertical gradients of *values*-dissolved iron in a. (o-red) and phosphate in b. (x-blue). *Only*

843 downgradient values are shown, which excludes several  $\text{PO}_4$ - and nearly all DFe-gradient  
844 values due to near-surface increased values (cf. Fig. 6e, 32°N profile). (d). Upward  
845  $\text{vV}$ ertical turbulent fluxes of phosphate concentration gradients in c. using average surface  
846  $K_z$  from Fig. 5b, valid for the depth average (here, ~17 m) of depths in a.  
847

Formatted: Subscript

Formatted: Font: Italic

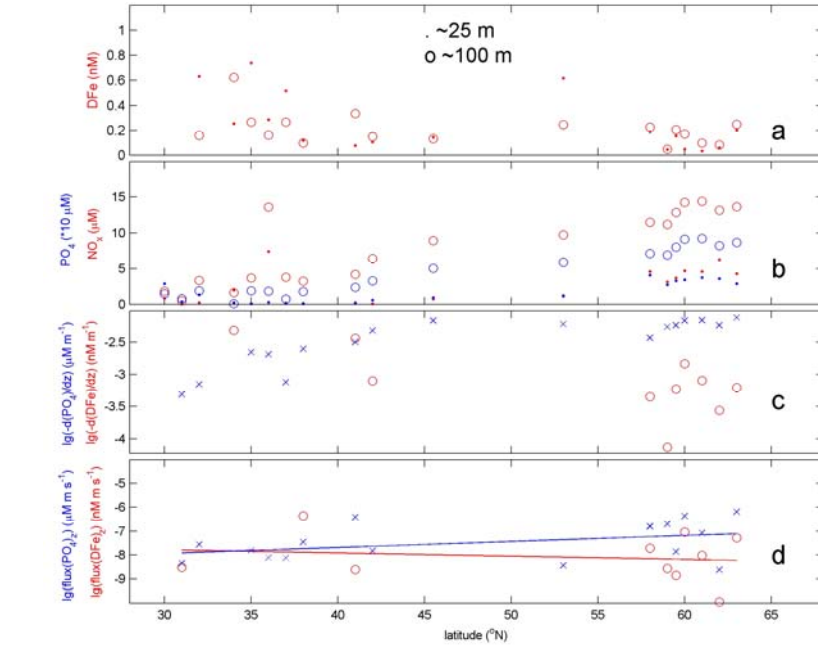
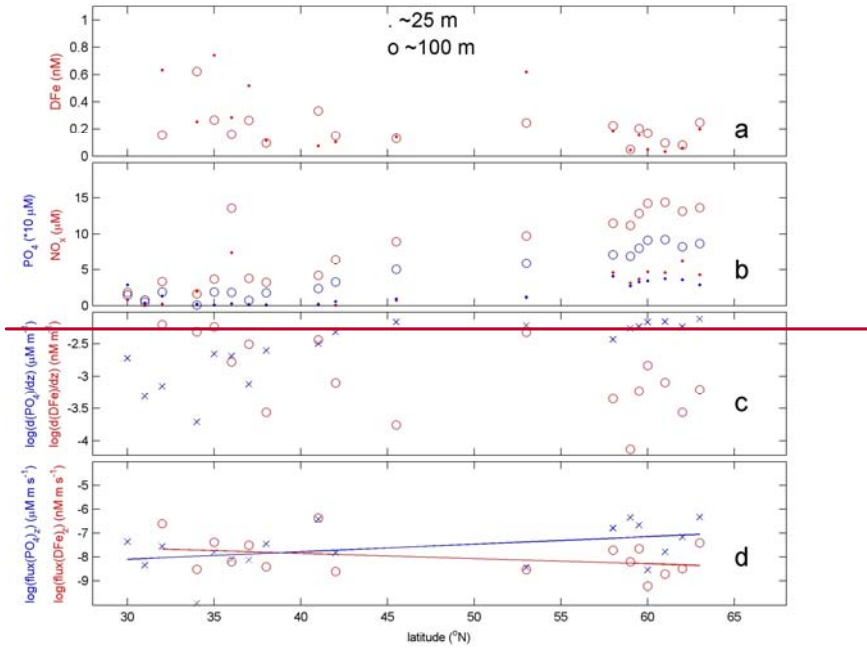
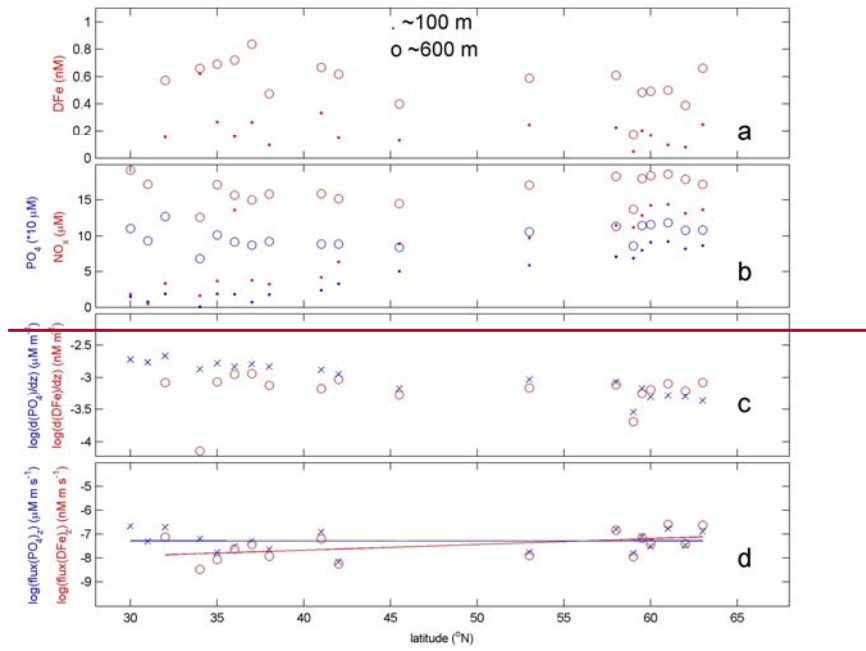
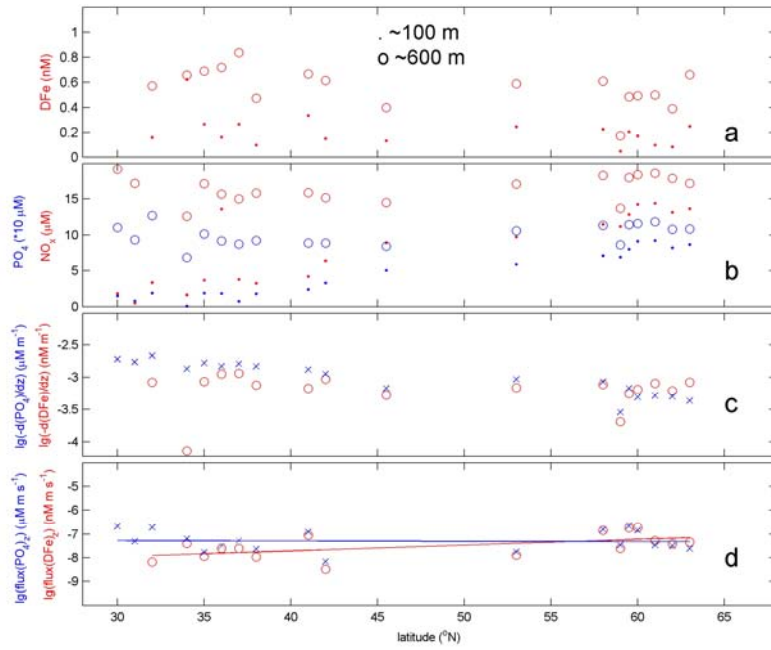


Figure 9. As Fig. 8, but for  $-100 < z < -25$  m, with fluxes for  $\sim 62$  m in d.

852



853



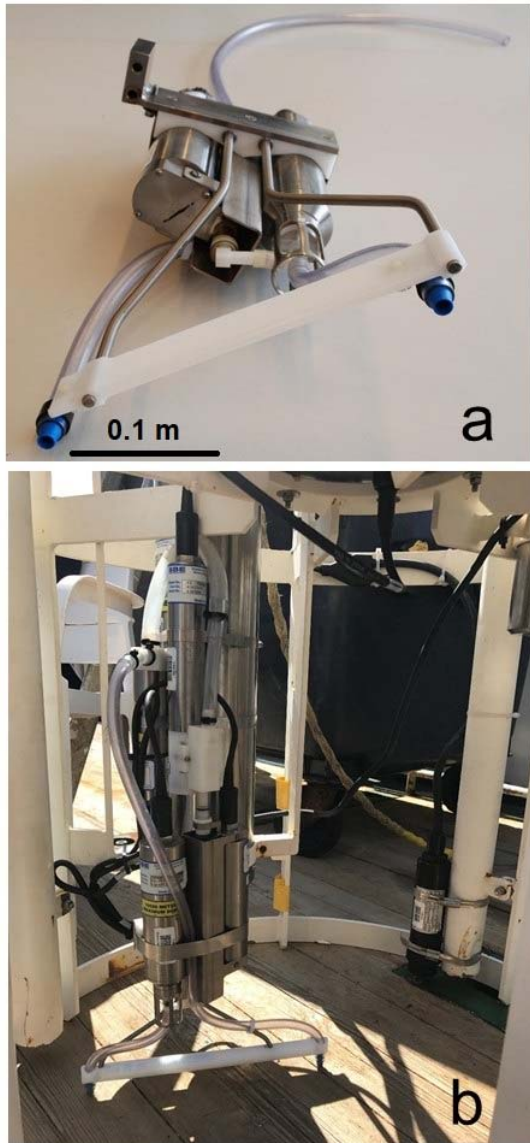
854

855

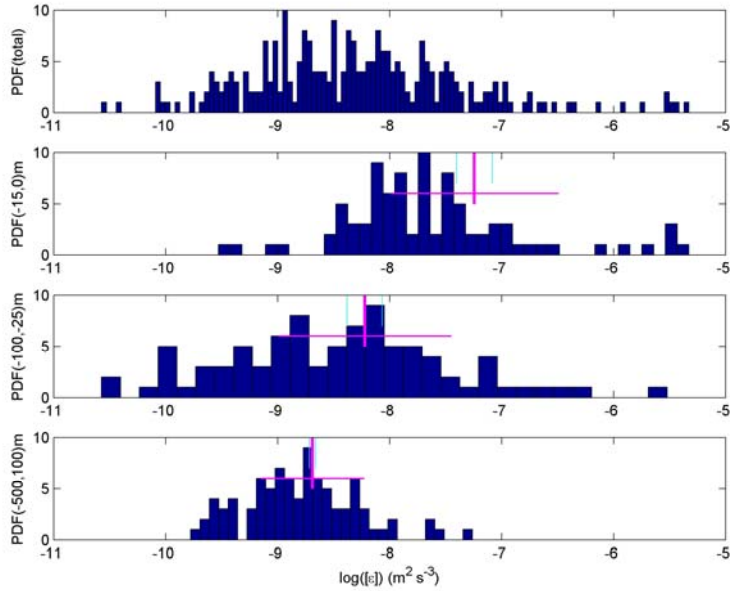
856

857

**Figure 10.** As Fig. 8, but for  $-600$  (few nutrients sampled at  $500$ )  $< z < -100$  m, with fluxes for  $\sim 350$  m in d.



858  
859 **Fig. A1.** SBE911 CTD-pump in- and outlet modification following the findings in van  
860 Haren and Laan (2016). (a) The T- and C-sensors clamped together with a structure holding  
861 in- and outlet pump-tubing of exactly the same diameter, separated at 0.3 m distance in the  
862 horizontal plane. (b) The modification of a. mounted in the CTD-frame.  
863



864  
 865 **Fig. A2.** Probability Density Functions of logarithm of vertically averaged dissipation rate  
 866 in comparison with latitudinal trend extreme values. (a) Distribution as a function of  
 867 latitude for all data. (b) As a, but for the upper 15 m averages only. The mean value is given  
 868 by the vertical purple line, with the horizontal line indicating  $\pm 1$  standard deviation. The  
 869 vertical light-blue lines indicate the best-fit value of the trend for  $30^\circ$  and  $63^\circ\text{N}$ . (c) As b,  
 870 but for averages between  $-100 < z < -25$  m. (d) As c, but for averages between  $-500 < z <$   
 871  $-100$  m.

100 m.